Lattice Distortions and Multiple Valence Band Convergence Contributing to High Thermoelectric performance in MnTe

Wenjie Xiong[1,#], Zhichao Wang[2#], Xuemei Zhang[3], Chong Wang[1], Liangcao Yin[4], Yaru Gong[1], Qingtang Zhang[1], Shuang Li[1], Qingfeng Liu[4], Peng Wang[2,*], Yongsheng Zhang[5,*], Guodong Tang[1,*]

[1]MIIT Key Laboratory of Advanced Metallic and Intermetallic Materials Technology, School of Materials Science and Engineering, Nanjing University of Science and Technology, Nanjing 210094, China.

[2]National Laboratory of Solid State Microstructures, College of Engineering and Applied Sciences and Collaborative, Innovation Center of Advanced Microstructures, Nanjing University, Nanjing 210093, China

[3]Key Laboratory of Materials Physics, Institute of Solid State Physics, Chinese Academy of Sciences, Hefei 230031, China.

[4]State Key Laboratory of Materials-Oriented Chemical Engineering, College of Chemical Engineering, Nanjing Tech University, Nanjing 211816, China.

[5]Advanced Research Institute of Multidisciplinary Sciences, Qufu Normal University, Qufu, Shandong Province, 273165, China.

* To whom correspond should be addressed.

E-mail: tangguodong@njust.edu.cn (G.T.).

yshzhang@qfnu.edu.cn (Y.Z.).

wangpeng@nju.edu.cn (P.W.).

# These authors contribute equally to this work

ABSTRACT

Here, a new route is proposed for the minimization of lattice thermal conductivity in MnTe through considerable increasing phonon scattering by introducing dense lattice distortions. Dense lattice distortions can be induced by Cu and Ag dopants possessing large differences in atom radius with host elements, which causes strong phonon scattering and results in extremely low lattice thermal conductivity. DFT calculations reveal that Cu and Ag codoping enables multiple valence band convergence and produces a high density of state values in the electronic structure of MnTe, contributing to the large Seebeck coefficient. Cu and Ag codoping not only optimizes the Seebeck coefficient but also substantially increases the carrier concentration and electrical conductivity, resulting in the significant enhancement of power factor. The maximum power factor reaches 11.36 $\mu Wcm^{-1}K^{-2}$ in $Mn_{0.98}Cu_{0.04}Ag_{0.04}Te$. Consequently, an outstanding *ZT* of 1.3 is achieved for $Mn_{0.98}Cu_{0.04}Ag_{0.04}Te$ by these synergistic effects. This study provides guidelines for developing high-performance thermoelectric materials through the rational design of effective dopants.

INTRODUCTION

Thermoelectric (TE) materials can realize the reversibly direct conversion of heat and electrical energy without moving parts and noise, which have unique advantages in energy harvesting and solid-state refrigeration.[1–3] The energy conversion efficiency of a thermoelectric material depends on the dimensionless figure of merit ZT defined as $ZT=S^2\sigma T/(\kappa_e + \kappa_L)$, where S is the Seebeck coefficient, σ is the electrical conductivity, κ_e is the electronic thermal conductivity, κ_L is the lattice thermal conductivity and T is absolute temperature.[4,5] High thermoelectric conversion efficiency requires high power factor $S^2\sigma$ and low thermal conductivity κ_T. However, it is challenging to decouple the intrinsic connection between thermoelectric parameters for maximizing the final ZT and energy conversion efficiency. Band structure engineering,[6–8] resonant levels,[9–11] phonon anharmonicity,[12–14] all-scale hierarchical architecture[15–17] and nanostructuring[18–20] have been demonstrated to be very effective for optimizing thermoelectric performance in different thermoelectric systems including GeTe,[21] PbTe,[22] Mg_2Si,[23] SnSe,[24–27] $AgSnSbSe_3$, SnTe,[28–30] Cu_2Se,[31,32] and half-Heusler alloys.[33,34]

Among chalcogenide semiconductors, the lead-free MnTe compound is expected to be a potential medium-temperature thermoelectric material due to its

environmentally friendly constituent and earth-abundant elements.[35] MnTe is a p-type semiconductor with a crystal structure of the NiAs type, which has a direct band gap of 1.27 eV and an indirect band gap of 0.8 eV at room temperature.[36] Such a band gap width can ensure reasonable electrical conductivity while reducing the adverse effect of bipolar effect on the Seebeck coefficient.[37] Due to the high structural symmetry and flattening of the top of the valence band, pristine MnTe exhibits a high Seebeck coefficient and a large DOS effective mass, making it a promising thermoelectric material.[38] However, the strong optical phonon scattering deteriorates the carrier mobility due to the large electronegativity difference between Mn (1.55) and Te (2.10).[35] Its low carrier mobility (~6 $cm^2 V^{-1} s^{-1}$) and low carrier concentration (~$10^{18} cm^{-3}$) result in inferior thermoelectric performance in MnTe.[39]

Various strategies have been explored to improve the thermoelectric performance of MnTe. Chemical doping, replacing Mn at the cation site with a hetero valent metal (e.g., Li,[40] Na,[41] Ag,[42] Cu,[43] Sb[38]) or Te at the anion site with an equivalent element (e.g., S,[37] Se[44]) was demonstrated as effective approach for enhance thermoelectric performance by modulating the carrier concentration. Xu et al. reported a ZT of 1.0 at 873 K by substituting Mn with Na.[42] Introducing high density of dislocations[45] and nanostructuring[41] have been proved as effective methods to reduce lattice thermal

conductivity because of the enhanced phonon scattering. Although optimizing the carrier concentration can greatly improve the electrical conductivity, it also severely deteriorates the Seebeck coefficient. No remarkable improvement can be achieved in power factor due to the strong coupling between the electrical conductivity and Seebeck coefficient. There is still a huge room to reduce lattice thermal conductivity because most of the reported doped MnTe maintains high lattice thermal conductivity.

In this study, effective Cu and Ag dopants were used to significantly enhance the thermoeletric performance of MnTe. Cu and Ag dopants, which possess large differences in atom radii with host Mn element, can introduce dense lattice distortions into MnTe matrix. Dense lattice distortions result in ultralow lattice thermal conductivity through strengthening phonon scattering. The multiple valence band convergence promoted by the Cu and Ag doping elements contributes to the large Seebeck coefficient. The electrical conductivity increases due to significant enhancement of carrier concentration. We achieve remarkable improvement in power factor by decoupling electrical conductivity and Seebeck coefficient. As a result, a remarkably high *ZT* of 1.3 was achieved for $Mn_{0.98}Cu_{0.04}Ag_{0.04}Te$ at 873 K. The synergy of multiple valence band convergence and lattice distortions provides a new pathway for designing prospective thermoelectrics.

EXPERIMENTAL SECTION

The powders of highly pure manganese (99.99%), tellurium (99.99%), copper (99.99%) and silver (99.99%) elements were first stoichiometrically weighed according to the nominal compositions of $Mn_{1.06-2x}Cu_xAg_xTe$ (x=0, 0.02, 0.04, 0.06, 0.1) and then sealed in vacuum quartz tubes. The addition of extra 6 % Mn helps to reduce the production of the second phase of $MnTe_2$.[45] The tubes were heated to 1273 K in 10 h, soaked for 30 h and then rapidly cooled to room temperature by water quenching. The synthesized ingots were manually ground into fine powder by using a mortar and then sintered by the spark plasma sintering (SPS) method ((HPD 10, FCT System GmbH)) in vacuum at 873 K for 6 min under an axial compressive stress of 50 MPa.

X-ray diffraction (D8 Advance, Bruker, Germany) with Cu-Kα radiation was performed on the power samples. A high-resolution Scanning electron microscope Geminisem 500 was used to characterize the morphology of $Mn_{1.06-2x}Cu_xAg_xTe$ samples and its built-in energy dispersive spectrometer was used to obtain energy dispersive x-ray spectroscopy (EDS) mappings. High-angle annular dark-field scanning transmission electron microscopy (HAADF STEM) images were acquired on a FEI Titan G2 60-300 STEM.

The Seebeck coefficient (S) and electrical conductivity (σ) from 300 to 873K were

measured in the helium atmosphere with the Ulvac-Riko ZEM-3 instrument system. Thermal diffusivity (D) from 300 to 873K was measured in argon with a laser flasher (Netzsch LFA-457). Both the thermal and electrical transport properties of the samples were measured along the pressing direction. The specific heat capacity (C_p) was taken from the reference.[39] The densities (ρ) of the bulk samples were obtained by using Archimedes method on a density meter (ME204E). The thermal conductivity (κ) was derived from the formula $\kappa = DC_p\rho$. The Hall coefficient (R_H) was measured on a Hall measuring instrument (HMS-3000) by the van der Pauw method. The room-temperature Hall carrier concentration (n) was obtained by formula $n = 1/(eR_H)$ and mobility (μ) was obtained by the relationship of $\mu = \sigma R_H$. The uncertainty of measurement for electrical conductivity and Seebek coefficient is 5%, total thermal conductivity is 12%. The total uncertainty of the calculated ZT is about 20%.

The density functional theory calculations (DFT) are performed with the projector augmented wave (PAW) method as implemented in the Vienna ab initio simulation package (VASP).[46–48] The generalized gradient approximation (GGA) with the parametrization of Perdew, Burke, Ernzerhof (PBE) is used for the electronic exchange-correlation (EXC) function.[49] The plane-wave expansion kinetic energy cutoff of 450 eV is found to be sufficient for the total energy convergence 10^{-5} eV. To obtain the

reliably electrical properties, the spin-polarized calculation is included in the MnTe compound. To illustrate the effects of Cu and Ag doping on the electrical properties of MnTe, a large (4 × 4 × 2) MnTe supercell (a = 16.58 Å, b = 16.58 Å, c = 13.42 Å, containing 64 cations and 64 anions) is built to simulate the experimentally suggested doping concentrations. Based on the experimentally suggested the doping concentrations of Cu (4%) and Ag (4%) with the highest zT values, we construct the $Mn_{0.908}Cu_{0.046}Ag_{0.046}Te$, $Mn_{0.954}Cu_{0.046}Te$ and $Mn_{0.954}Cu_{0.046}Te$ supercells to simulate the electronic properties of Cu and Ag codoped MnTe compound. Since the Cu and Ag concentration we considered is 4.6% each, totally ~10%. Such high doping concentration would modify the band structures of MnTe. We test all possible configurations of Cu and Ag doping in the MnTe matrix, and select the most stable one depicted in Figure S1. Brillouin zones are sampled using a (15 × 15 × 10) and (3 × 3 × 3) Monkhorst-Pack[50] k-point grid for the pristine and supercell MnTe systems, respectively. The geometry structures are fully optimized until all the forces and components of the stress tensor are below 0.01 eV/Å^2 and 0.2 kbar, respectively. Considering the created supercell structure results from the pristine primitive cell, the band folding is inevitable in the band structure of it. Then, we apply a band unfolding methodology (the BandUP code) along the high symmetry directions of the primitive

cell and then recover the effective primitive picture.[51]

RESULTS AND DISCCUSSION

Powder X-ray diffraction (XRD) patterns of $Mn_{1.06-2x}Cu_xAg_xTe$ samples are shown in **Figure** 1. The majority of the diffraction peaks of all samples can be well indexed to the MnTe standard card (PDF#18-0814) with hexagonal symmetry (P63/mmc space group). A small amount of $MnTe_2$ impurity phase was observed as the doping level *x* reaches above 0.06. Lattice parameters extracted from XRD cell refinement increase with raising the Ag and Cu content (**Figure** 1b), which can be ascribed to larger ion radius of Ag^+ (126 pm) and Cu^+ (77 pm) than Mn^{2+} (66 pm). Energy dispersive spectroscopy (EDS) elemental mapping clearly indicates the uniform distribution for individual elements (Figure S2). No evidence of silver- or copper-rich second phases can be found, which suggests that Ag and Cu are fully dissloved into the lattices of MnTe. High density of micro/nanopores can be observed in the sample (Figure S2a). Micro/nanopores can be clearly found in the fracture surface of $Mn_{0.98}Cu_{0.04}Ag_{0.04}Te$ sample (Figure S3). The relative densities of bulk samples reach above 90% (Table S1).

The temperature dependence of electrical conductivities (σ) for $Mn_{1.06-2x}Cu_xAg_xTe$ samples are shown in **Figure** 2a. As temperature increases, compared with the pristine $Mn_{1.06}Te$, σ of $Mn_{1.06-2x}Cu_xAg_xTe$ samples enhance considerably in the whole

temperature range. In particular, σ of $Mn_{1.02}Cu_{0.02}Ag_{0.02}Te$ reaches a maximum value of 17731 S m^{-1} at 873 K, which is more than three times higher than that of pristine $Mn_{1.06}Te$ (5700 S m^{-1}). σ of Ag and Cu codoped $Mn_{1.06}Te$ samples decreases with elevating temperature in the temperature of 300-523 K, showing a heavily doped semiconductor behavior.[52] It then increases sharply above 523 K because of well-known intrinsic excitation.[37] The Hall carrier concentration and mobility were measured to further investigate the electrical transport behavior. Room temperature carrier concentration (n_H) is greatly enhanced after Ag and Cu codoping as compared to the pristine $Mn_{1.06}Te$ (**Figure** 2b). n_H first increases and then decreases with the increase of Cu and Ag doping content. Notably, $Mn_{0.98}Cu_{0.04}Ag_{0.04}Te$ shows the highest n_H of 2.48×10^{20} cm^{-3}, which is two orders of magnitude higher than pristine $Mn_{1.06}Te$ (5.5×10^{18} cm^{-3}). The slight decrease of n_H for $x>0.04$ can be attributed to the presence of $MnTe_2$ second phase. The formation of $MnTe_2$ will lead to non-stoichiometry of Te and deficiency, thereby reducing hole concentration. The carrier mobility gradually decreases with the increase of Cu and Ag doping content because of enhanced point defect scattering induced by Ag and Cu codoping. Therefore, the substantial enhancement of σ for $Mn_{1.06-2x}Cu_xAg_xTe$ samples mainly originates from the significant increase of n_H.

Figure 2c presents the temperature dependence of the Seebeck coefficient (*S*) for $Mn_{1.06-2x}Cu_xAg_xTe$ samples. Cu and Ag codoped samples show lower *S* than that of pristine $Mn_{1.06}Te$ over the entire temperature range. It is observed that *S* exhibits the same temperature-dependence trend for all $Mn_{1.06-2x}Cu_xAg_xTe$ samples. *S* first increases to a peak at around 600 K and then begins to decrease with the increase in temperature. The peak of *S* indicate the onset of bipolar conduction behavior after Cu and Ag codoping.[35] However, the peaks of the Cu and Ag codoped MnTe shift to a higher temperature compared with that of undoped $Mn_{1.06}Te$, which are attributed to the enlarging band gap (Table 1). Bipolar carrier diffusion gives rise to minority carriers (electrons), which deteriorates *S* in the intrinsic temperature range. The Pisarenko relationship between the Seebeck coefficient (*S*) and the carrier concentration (n_H) reveals band structure modification by Ag and Cu incorporation. As shown in **Figure** 3a, the experimental data of previously reported undoped and Na, Cu doped MnTe[35,41,43] fall on the theoretical Pisarenko line, demonstrating the validity of the SPB model for MnTe.[53] Cu and Ag doped samples shows higher *S* than the Pisarenko line, indicating that introduction of Cu and Ag modify the band structure of MnTe.

To explore the underlying reasons for the enhanced thermoelectric performance of Cu and Ag codoped MnTe, we further examine their electronic band structures. Due to

the well-known of underestimated the band gap in the PBE calculations, we corrected the PBE calculated MnTe band structures using the HSE (Heyd–Scuseria–Ernzerhof) calculations, as following the strategy used in Ref.[35]. **Figure** 3b displays the corrected band structures of pristine MnTe compound, the band gap is 0.71 eV and the energy differences of valence band maxima of $\Delta E(\Gamma\text{-}M)$, $\Delta E(\Gamma\text{-}H)$ and $\Delta E(\Gamma\text{-}A)$ are 0.04, 0.26 and 0.34 eV in Table 1, respectively, which are very close to the HSE results in Ref. [35]. We found that Cu or Ag single doping shows an evident convergence effect of the valance bands (Γ, H and A high symmetry points in **Figure** 3c and **Figure** 3d) as compared with pristine MnTe. **Figure** 3e depicts the unfolded band structures of supercells constructed by experimental doping concentration ($Mn_{0.908}Cu_{0.046}Ag_{0.046}Te$). It is obvious that Cu (~4%)-Ag (~4%) codoped MnTe matrix shows an evident convergence effect of the valance bands (Γ, H and A high symmetry points in **Figure** 3e): the energy difference of $\Delta E(\Gamma\text{-}M)$, $\Delta E(\Gamma\text{-}H)$ and $\Delta E(\Gamma\text{-}A)$ decreases to 0.04, 0.17 and 0.12 eV, respectively, which is visibly smaller than the single doping effects of Cu or Ag in **Figure** 3c, d and Table 1. This indicates that Cu and Ag codoping can further converge valance bands of Cu or Ag single doped MnTe. The high valance band degeneracy generates the steeply increased DOS around the Fermi level (Figure 3f) and would enhance the Seebeck coefficient. DFT calculations reveal that Cu and Ag

codoping enables multiple valence band convergence and produce a high DOS values in the electronic structure of MnTe, contributing to the large Seebeck coefficient in Cu and Ag codoped MnTe.

The temperature dependence of power factor (PF) for $Mn_{1.06-2x}Cu_xAg_xTe$ samples is shown in **Figure** 2d. Compared to pristine $Mn_{1.06}Te$, the power factor of Cu- and Ag-doped samples increases significantly over the entire temperature range due to the increase in carrier concentration. A PF of 11.36 $\mu Wcm^{-1} K^{-2}$ is achieved at 873 K for heavily Cu- and Ag-doped $Mn_{0.98}Cu_{0.04}Ag_{0.04}Te$ with high thermoelectric performance, which is increased by ~92% compared to that of pure $Mn_{1.06}Te$ (5.93 $\mu Wcm^{-1} K^{-2}$). Although the Seebeck coefficient decreases after doping, the greatly improved conductivity results in a significant increase in the power factor of the final doped Cu and Ag samples.

The total thermal conductivity (**κ_T**) for $Mn_{1.06-2x}Cu_xAg_xTe$ samples as a function of temperature is presented in **Figure** 4a. κ_T of $Mn_{1.06-2x}Cu_xAg_xTe$ is suppressed as compared with $Mn_{1.06}Te$ below 673 K. Above 673 K, κ_T of $Mn_{1.06-2x}Cu_xAg_xTe$ (x>0.04) is larger than that of $Mn_{1.06}Te$ (**Figure** 4a). This can be ascribed to larger contribution of the electronic thermal conductivity (κ_e) due to the sharp increase of electrical conductivity at high temperature. κ_e is calculated based on the Wiedemann−Franz

relation, $\kappa_e = L\sigma T$, where L is the Lorenz number, σ is the electrical conductivity and T is absolute temperature. Considering acoustic phonon scattering, The Lorenz number (L) is calculated by fitting the Seebeck coefficient values with an assumption of a single-band model,[54,55] as illustrated in Figure S4. κ_e of the Cu and Ag codoped samples are significantly higher than that of pristine $Mn_{1.06}Te$ throughout the temperature range due to enhanced σ (**Figure** 4b). The lattice thermal conductivity (κ_L) was calculated by subtracting κ_e from κ_T. κ_L of the Cu and Ag codoped samples (**Figure** 4c) is obviously lower than that of pristine $Mn_{1.06}Te$. The $Mn_{0.98}Cu_{0.04}Ag_{0.04}Te$ sample exhibits the lowest κ_L among all Cu- and Ag-doped samples. An ultralow κ_L of $\approx$0.55 W m^{-1} K^{-1} is obtained in the composition of $Mn_{0.98}Cu_{0.04}Ag_{0.04}Te$ at 873 K, and this value is remarkably decreased compared with that of pristine $Mn_{1.06}Te$ (0.77 W m^{-1} K^{-1}). κ_L increases as Cu and Ag doping level x reach above 0.04. The presence of $MnTe_2$ exhibiting high lattice thermal conductivity induces the enhanced κ_L.[56]

The microstructure analysis of the typical $Mn_{0.98}Cu_{0.04}Ag_{0.04}Te$ sample was carried out on a FEI Titan G2 60-300 STEM equipped with double aberration correctors to investigate the underlying mechanism of the reduction in κ_L. Nanoprecipitates appearing as dark quasi-circular shape can be clearly observed in the MnTe matrix (**Figure** 5a and 5b). The locations of these nanoprecipitates are coincident with the Mn

enrichment areas as shown in the STEM-EDS elemental mappings, which indicates the dark domains are Mn-rich nanoprecipitates.[57–59] Atomically resolved HAADF-STEM images of the nanoprecipitate (**Figure** 5c) and matrix phase (Figure S5) are obtained, indicating obviously different atomic structures for the MnTe matrix and nanoprecipitate. In addition to Mn-rich nanoprecipitates, dislocations (marked with T) can be clearly found in the matrix, which are indicated as yellow symbols (**Figure** 5d and Figure. S6). Dense lattice distortions were induced by Ag and Cu codoping, as illustrated in HAADF-STEM image (**Figure** 5e and S7a). To analyze the lattice strain induced by lattice distortions, geometric phase analysis (GPA) was performed on the corresponding HAADF-STEM image. GPA is a semi-quantitative lattice image processing method that can reveal spatially distributed strain fields. The corresponding strain maps and distributions can be found in **Figure** 5f and Figure S7b. Larger fluctuations in average lattice strain indicate a broader distribution of static lattice strain around lattice distortions. Ag and Cu dopants possesses large differences in atom radius with the host Mn elements, as illustrated in **Figure** 4d. Dense lattice distortions are induced by the large difference in atom radius between dopants and host atoms. Dense lattice distortions cause strong phonon scattering and significantly depress the κ_L. Furthermore, large mass fluctuation can be induced by Ag and Cu codoping, as shown

in Fig. 4d. Theoretically, the κ_L can be calculated as:[60,61]

$$\kappa_L = \frac{1}{3}\int_0^{\omega_0} C_v(\omega) v^2 \tau d\omega \quad (1)$$

where C_v is the specific heat, v is the phonon velocity, ω is the angular frequency, ω_0 is the cut-off frequency, and τ is the phonon scattering relaxation time, which is expressed as:[62–64]

$$\tau^{-1} = \tau_\varepsilon^{-1} + \tau_M^{-1} = \gamma^2\varepsilon^2 + (\frac{\Delta M}{M})^2 \quad (2)$$

γ is the Grüneisen parameter, ε is the static lattice strain and $\Delta M/\bar{M}$ is the mass fluctuations. Based on formula (2), the large mass fluctuation will shorten the phonon relaxation time, resulting in a reduction on κ_L. The increased interfaces arising from micro/nanopores cause strong phonon scattering[65,66]. Combining extra phonon scattering from Mn-rich nanoprecipitates and dislocations, $Mn_{0.98}Cu_{0.04}Ag_{0.04}Te$ sample shows significantly reduced κ_L.

The temperature-dependent *ZT* values for $Mn_{1.06-2x}Cu_xAg_xTe$ are presented in **Figure** 6a. The *ZT* value of $Mn_{1.06-2x}Cu_xAg_xTe$ samples increases with elevating temperature and is significantly enhanced compared with pristine $Mn_{1.06}Te$. An outstanding ZT of ~1.3 is achieved in $Mn_{0.98}Cu_{0.04}Ag_{0.04}Te$ at 873 K through decoupling electrical and thermal transport properties. Multiple valence band convergence and lattice distortions induced by large difference in atom radii between

dopants and host atoms successfully accumulate the ZT enhancement to 113%. Peak ZT of $Mn_{0.98}Cu_{0.04}Ag_{0.04}Te$ are one of the highest peak ZT for MnTe system reported so far[42,44,53,67–69] (**Figure** 6b).

CONCLUSIONS

In summary, we achieve high ZT of ~ 1.3 in Cu and Ag codoped MnTe thermoelectrics, deriving from markedly reduced lattice thermal conductivity and significantly increased *PF*. It is found that Cu and Ag dopants cause dense lattice distortions due to large differences in atom radii between the dopants and host elements. Combining Mn-rich nanoprecipitates and dislocations, dense lattice distortions lead to ultralow lattice thermal conductivity (0.55 W m^{-1} K^{-1}). Cu and Ag codoping achieves optimal carrier concentration and facilitates multiple valence band convergence and high density of states values in the electronic structure, which leads to sharp increase of power factor. The demonstrated strategy of screening suitable elements according to large atom redius difference for introducing dense lattice distortions highlights the importance of phonon engineering in advancing high-performance thermoelectrics.

CONFLICTS OF INTEREST

There is no conflict to declare.

ACKNOWLEDGEMENTS

The work was supported by the National Natural Science Foundation of China (No. 52071182), the “Qinglan Project” of the Young and Middle-aged Academic Leader of Jiangsu Province, and the Fundamental Research Funds for the Central Universities (No. 30921011107).

REFERENCES

[1] G. J. Snyder, E. S. Toberer, *Nat. Mater.* **2008**, *7*, 105.

[2] I. Petsagkourakis, K. Tybrandt, X. Crispin, I. Ohkubo, N. Satoh, T. Mori, *Sci. Technol. Adv. Mater.* **2018**, *19*, 836.

[3] Y. Wang, L. Yang, X. Shi, X. Shi, L. Chen, M. S. Dargusch, J. Zou, Z. Chen, *Adv. Mater.* **2019**, *31*, 1807916.

[4] G. Tan, L.-D. Zhao, M. G. Kanatzidis, *Chem. Rev.* **2016**, *116*, 12123.

[5] Y. Xiao, J. Yang, Q. Jiang, L. Fu, Y. Luo, M. Liu, D. Zhang, M. Zhang, W. Li, J. Peng, F. Chen, *J. Mater. Chem. A* **2014**, *2*, 20288.

[6] X. Li, J. Liu, S. Li, J. Zhang, D. Li, R. Xu, Q. Zhang, X. Zhang, B. Xu, Y. Zhang, F. Xu, G. Tang, *Nano Energy* **2020**, *67*, 104261.

[7] Y. Pei, X. Shi, A. LaLonde, H. Wang, L. Chen, G. J. Snyder, *Nature* **2011**, *473*, 66.

[8] M. Hong, Z.-G. Chen, L. Yang, T. C. Chasapis, S. D. Kang, Y. Zou, G. J. Auchterlonie, M. G. Kanatzidis, G. J. Snyder, J. Zou, *J. Mater. Chem. A* **2017**, *5*, 10713.

[9] G. Tan, W. G. Zeier, F. Shi, P. Wang, G. J. Snyder, V. P. Dravid, M. G. Kanatzidis, *Chem Mater* **2015**, *27*, 7801.

[10] L. Wu, X. Li, S. Wang, T. Zhang, J. Yang, W. Zhang, L. Chen, J. Yang, *NPG Asia Mater* **2017**, *9*, e343.

[11] M. Hong, Z. Chen, L. Yang, Y. Zou, M. Dargusch, H. Wang, J. Zou, *Adv. Mater.* **2018**, *30*, 1705942.

[12] O. Delaire, J. Ma, K. Marty, A. F. May, M. A. McGuire, M.-H. Du, D. J. Singh, A. Podlesnyak, G. Ehlers, M. D. Lumsden, B. C. Sales, *Nat. Mater.* **2011**, *10*, 614.

[13] S. Lee, K. Esfarjani, T. Luo, J. Zhou, Z. Tian, G. Chen, *Nat. Commun.* **2014**, *5*, 3525.

[14] W. Qiu, L. Xi, P. Wei, X. Ke, J. Yang, W. Zhang, *Proc. Natl. Acad. Sci.* **2014**, *111*, 15031.

[15] L. D. Zhao, H. J. Wu, S. Q. Hao, C. I. Wu, X. Y. Zhou, K. Biswas, J. Q. He, T. P. Hogan, C. Uher, C. Wolverton, V. P. Dravid, M. G. Kanatzidis, *Energy Environ. Sci.* **2013**, *6*, 3346.

[16] K. Biswas, J. He, I. D. Blum, C.-I. Wu, T. P. Hogan, D. N. Seidman, V. P. Dravid, M. G. Kanatzidis, *Nature* **2012**, *489*, 414.

[17] P. Jood, M. Ohta, *Mater. Basel Switz.* **2015**, *8*, 1124.

[18] E. K. Chere, Q. Zhang, K. Dahal, F. Cao, J. Mao, Z. Ren, *J. Mater. Chem. A* **2016**, *4*, 1848.

[19] J. Dong, J. Pei, H.-L. Zhuang, H. Hu, B. Cai, J.-F. Li, *J. Mater. Chem. A* **2019**, *7*, 27361.

[20] J. Liu, P. Wang, M. Wang, R. Xu, J. Zhang, J. Liu, D. Li, N. Liang, Y. Du, G. Chen, G. Tang, *Nano Energy* **2018**, *53*, 683.

[21] X. Zhang, Z. Bu, S. Lin, Z. Chen, W. Li, Y. Pei, *Joule* **2020**, *4*, 986.

[22] J. P. Heremans, V. Jovovic, E. S. Toberer, A. Saramat, K. Kurosaki, A. Charoenphakdee, S. Yamanaka, G. J. Snyder, *Science* **2008**, *321*, 554.

[23] W. Liu, K. Yin, Q. Zhang, C. Uher, X. Tang, *Natl. Sci. Rev.* **2017**, *4*, 611.

[24] X. Lou, S. Li, X. Chen, Q. Zhang, H. Deng, J. Zhang, D. Li, X. Zhang, Y. Zhang, H. Zeng, G. Tang, *ACS Nano* **2021**, *15*, 8204.

[25] W. Lu, S. Li, R. Xu, J. Zhang, D. Li, Z. Feng, Y. Zhang, G. Tang, *ACS Appl. Mater. Interfaces* **2019**, *11*, 45133.

[26] L.-D. Zhao, S.-H. Lo, Y. Zhang, H. Sun, G. Tan, C. Uher, C. Wolverton, V. P. Dravid, M. G. Kanatzidis, *Nature* **2014**, *508*, 373.

[27] T. Hussain, X. Li, M. H. Danish, M. U. Rehman, J. Zhang, D. Li, G. Chen, G. Tang, *Nano Energy* **2020**, *73*, 104832.

[28] Z. Zhou, J. Yang, Q. Jiang, Y. Luo, D. Zhang, Y. Ren, X. He, J. Xin, *J. Mater. Chem. A* **2016**, *4*, 13171.

[29] Z. Zhou, J. Yang, Q. Jiang, X. Lin, J. Xin, A. Basit, J. Hou, B. Sun, *Nano Energy* **2018**, *47*, 81.

[30] Y. Liu, X. Zhang, P. Nan, B. Zou, Q. Zhang, Y. Hou, S. Li, Y. Gong, Q. Liu, B. Ge, O. Cojocaru-Mirédin, Y. Yu, Y. Zhang, G. Chen, M. Wuttig, G. Tang, *Adv. Funct. Mater.* **2022**, *n/a*, 2209980.

[31] W.-D. Liu, L. Yang, Z.-G. Chen, *Nano Today* **2020**, *35*, 100938.

[32] L. Chen, J. Liu, C. Jiang, K. Zhao, H. Chen, X. Shi, L. Chen, C. Sun, S. Zhang, Y. Wang, Z. Zhang, *Adv Mater* **2019**, *31*, e1804919.

[33] R. J. Quinn, J.-W. G. Bos, *Mater. Adv.* **2021**, *2*, 6246.

[34] A. Nozariasbmarz, U. Saparamadu, W. Li, H. B. Kang, C. Dettor, H. Zhu, B. Poudel, S. Priya, *J Power Sources* **2021**, *493*, 229695.

[35] H. Deng, X. Lou, W. Lu, J. Zhang, D. Li, S. Li, Q. Zhang, X. Zhang, X. Chen, D. Zhang, Y. Zhang, G. Tang, *Nano Energy* **2021**, *81*, 105649.

[36] L. M. Sandratskii, R. F. Egorov, A. A. Berdyshev, *Phys. Status Solidi B* **1981**, *104*, 103.

[37] W. Xie, S. Populoh, K. Gałązka, X. Xiao, L. Sagarna, Y. Liu, M. Trottmann, J. He, A. Weidenkaff, *J. Appl. Phys.* **2014**, *115*, 103707.

[38] P. R. Sreeram, V. Ganesan, S. Thomas, M. R. Anantharaman, *J Alloys Compd* **2020**, *836*, 155374.

[39] Y. Luo, T. Xu, Z. Ma, D. Zhang, Z. Guo, Q. Jiang, J. Yang, Q. Yan, M. G.

Kanatzidis, *J Am Chem Soc* **2021**, *143*, 13990.

[40] Y. Zheng, T. Lu, M. M. H. Polash, M. Rasoulianboroujeni, N. Liu, M. E. Manley, Y. Deng, P. J. Sun, X. L. Chen, R. P. Hermann, D. Vashaee, J. P. Heremans, H. Zhao, *Sci. Adv.* **2019**, *5*, eaat9461.

[41] Y. Ren, J. Yang, Q. Jiang, D. Zhang, Z. Zhou, X. Li, J. Xin, X. He, *J. Mater. Chem. C* **2017**, *5*, 5076.

[42] Y. Xu, W. Li, C. Wang, J. Li, Z. Chen, S. Lin, Y. Chen, Y. Pei, *J. Mater. Chem. A* **2017**, *5*, 19143.

[43] Y. Ren, Q. Jiang, J. Yang, Y. Luo, D. Zhang, Y. Cheng, Z. Zhou, *J. Materiomics* **2016**, *2*, 172.

[44] J. Dong, F.-H. Sun, H. Tang, K. Hayashi, H. Li, P.-P. Shang, Y. Miyazaki, J.-F. Li, *ACS Appl. Mater. Interfaces* **2019**, *11*, 28221.

[45] J. Xin, J. Yang, Q. Jiang, S. Li, A. Basit, H. Hu, Q. Long, S. Li, X. Li, *Nano Energy* **2019**, *57*, 703.

[46] G. Kresse, J. Hafner, *Phys. Rev. B* **1993**, *47*, 558.

[47] G. Kresse, J. Furthmüller, *Comput. Mater. Sci.* **1996**, *6*, 15.

[48] G. Kresse, D. Joubert, *Phys. Rev. B* **1999**, *59*, 1758.

[49] J. P. Perdew, K. Burke, M. Ernzerhof, *Phys. Rev. Lett.* **1996**, *77*, 3865.

[50] H. J. Monkhorst, J. D. Pack, *Phys. Rev. B* **1976**, *13*, 5188.

[51] P. V. C. Medeiros, S. Stafström, J. Björk, *Phys. Rev. B* **2014**, *89*, 041407.

[52] X. She, X. Su, H. Xie, J. Fu, Y. Yan, W. Liu, P. F. Poudeu Poudeu, X. Tang, *ACS Appl. Mater. Interfaces* **2018**, *10*, 25519.

[53] J. Dong, C.-F. Wu, J. Pei, F.-H. Sun, Y. Pan, B.-P. Zhang, H. Tang, J.-F. Li, *J. Mater. Chem. C* **2018**, *6*, 4265.

[54] T.-R. Wei, H. Wang, Z. M. Gibbs, C.-F. Wu, G. J. Snyder, J.-F. Li, *J. Mater. Chem. A* **2014**, *2*, 13527.

[55] Y. Luo, J. Yang, G. Li, M. Liu, Y. Xiao, L. Fu, W. Li, P. Zhu, J. Peng, S. Gao, J. Zhang, *Adv. Energy Mater.* **2014**, *4*, 1300599.

[56] Y. Xu, W. Li, C. Wang, Z. Chen, Y. Wu, X. Zhang, J. Li, S. Lin, Y. Chen, Y. Pei, *J. Materiomics* **2018**, *4*, 215.

[57] G. Tang, J. Liu, J. Zhang, D. Li, K. Rara, R. Xu, W. Lu, J. Liu, Y. Zhang, Z. Peng, *ACS Appl. Mater. INTERFACES* **2018**, *10*, 30558.

[58] W. Wei, C. Chang, T. Yang, J. Liu, H. Tang, J. Zhang, Y. Li, F. Xu, Z. Zhang, J.-F. Li, G. Tang, *J. Am. Chem. Soc.* **2018**, *140*, 499.

[59] R. Xu, L. Huang, J. Zhang, D. Li, J. Liu, J. Liu, J. Fang, M. Wang, G. Tang, *J. Mater. Chem. A* **2019**, *7*, 15757.

[60] J. Callaway, *Phys. Rev.* **1959**, *113*, 1046.

[61] J. Callaway, H. C. von Baeyer, *Phys. Rev.* **1960**, *120*, 1149.

[62] G. A. Slack, *Phys. Rev.* **1957**, *105*, 829.

[63] B. Abeles, *Phys. Rev.* **1963**, *131*, 1906.

[64] S. Li, X. Lou, B. Zou, Y. Hou, J. Zhang, D. Li, J. Fang, T. Feng, D. Zhang, Y. Liu, J. Liu, G. Tang, *Mater. Today Phys.* **2021**, *21*, 100542.

[65] X. Shi, A. Wu, W. Liu, R. Moshwan, Y. Wang, Z.-G. Chen, J. Zou, *ACS Nano* **2018**, *12*, 11417.

[66] S. Li, Y. Hou, S. Zhang, Y. Gong, S. Siddique, D. Li, J. Fang, P. Nan, B. Ge, G. Tang, *Chem. Eng. J.* **2022**, 138637.

[67] J. Dong, J. Pei, K. Hayashi, W. Saito, H. Li, B. Cai, Y. Miyazaki, J.-F. Li, *J Mater* **2021**, *7*, 577.

[68] A. Basit, J. Yang, Q. Jiang, J. Xin, X. Li, S. Li, S. Li, Q. Long, *J. Mater. Chem. A* **2018**, *6*, 23473.

[69] A. Basit, J. Yang, Q. Jiang, Z. Zhou, J. Xin, X. Li, S. Li, *J Alloys Compd* **2019**, *777*, 968.

Table 1. Energy differences between four valence maxima (the Γ, M, H and A points in the BZ) and the calculated band gaps for pristine MnTe and $Mn_{0.908}Cu_{0.046}Ag_{0.046}Te$ samples.

	MnTe	$Mn_{0.954}Cu_{0.046}Te$	$Mn_{0.954}Ag_{0.046}Te$	$Mn_{0.908}Cu_{0.046}Ag_{0.046}Te$
$\Delta\varepsilon_{\Gamma\text{-}M}$	0.04	0.05	0.04	0.04
$\Delta\varepsilon_{\Gamma\text{-}H}$	0.26	0.20	0.19	0.17
$\Delta\varepsilon_{\Gamma\text{-}A}$	0.34	0.27	0.28	0.12
Band gap(eV)	0.71	0.87	0.86	0.91

Figure. 1. (a) The XRD patterns for $Mn_{1.06}Te$ and $Mn_{1.06-2x}Cu_xAg_xTe$ samples; (b) Calculated lattice parameters as a function of Cu and Ag content.

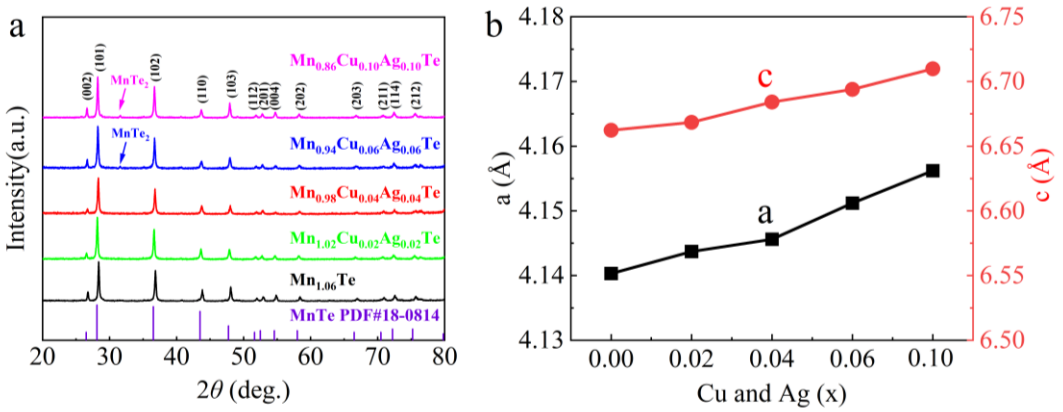

Figure. 2. (a) Temperature dependent electrical conductivity σ, (b) Carrier concentration n and carrier mobility μ at room temperature, (c) Temperature dependent Seebeck coefficient S, (d) Temperature dependent Power factor PF for $Mn_{1.06}Te$ and $Mn_{1.06-2x}Cu_xAg_xTe$.

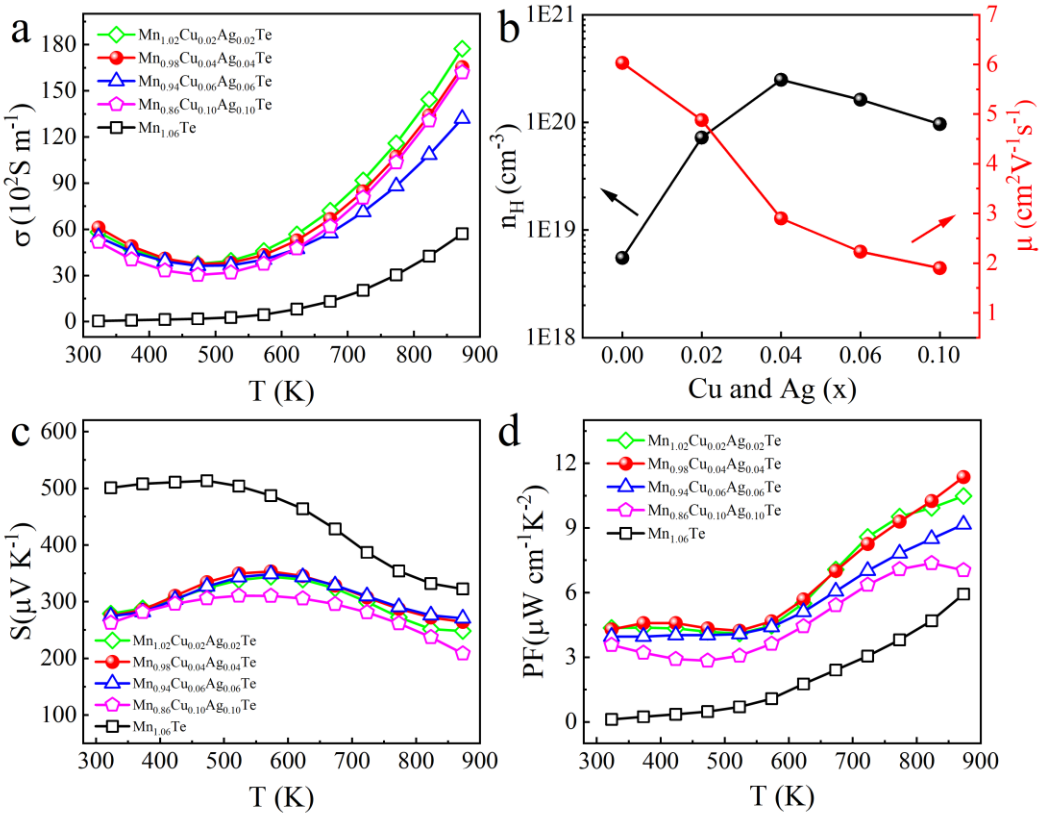

Figure. 3. (a) The carrier concentration dependent Seebeck coefficient of $Mn_{1.06-2x}Cu_xAg_xTe$ samples at room temperature and Pisarenko relation [53]. (b) The corrected PBE calculated electronic band structures of pristine MnTe based on HSE calculations. Electronic band structures of (c) $Mn_{0.954}Cu_{0.046}Te$, (d) $Mn_{0.954}Ag_{0.046}Te$, (e) $Mn_{0.908}Cu_{0.046}Ag_{0.046}Te$. The scale bar is the magnitude of the spectral weight, which characterizes the probability of the primitive cell eigenstates contributing to a particular supercell eigenstate of the same energy. (f) Electronic density of states of $Mn_{0.908}Cu_{0.046}Ag_{0.046}Te$. The insert panel zooms in the region around the Fermi level.

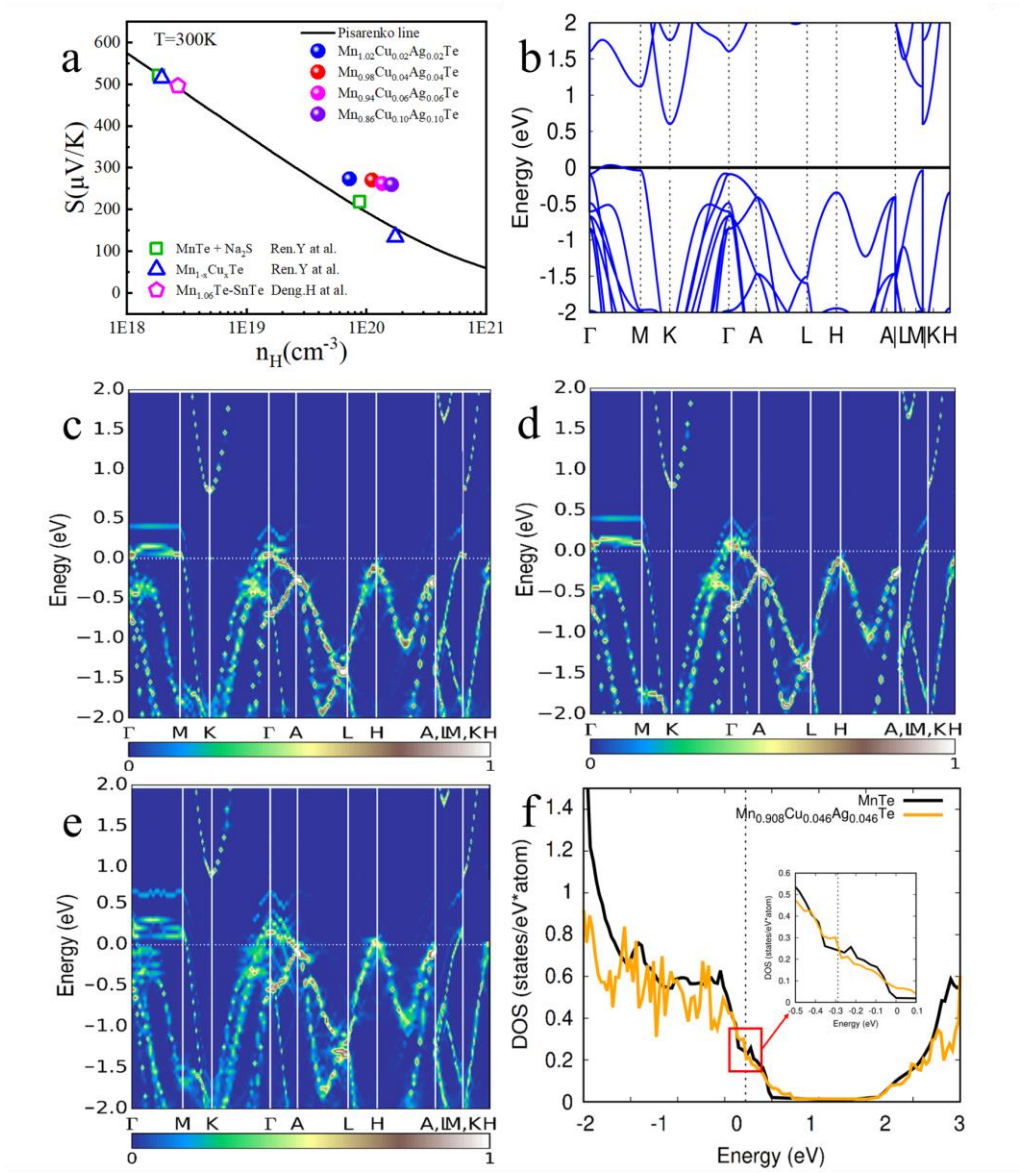

Figure. 4. Temperature dependent thermal transport properties for $Mn_{1.06}Te$ and $Mn_{1.06-2x}Cu_xAg_xTe$ samples:(a) Total thermal conductivity (κ_T), (b) Lattice thermal conductivity (κ_L), (c) Electronic thermal conductivity (κ_e) as a function of temperature for $Mn_{1.06}Te$ and $Mn_{1.06-2x}Cu_xAg_xTe$ samples, (d) Atom radius difference $\Delta r/\bar{r}$ and mass difference $\Delta M/\bar{M}$ of typical dopants in MnTe for comparison.

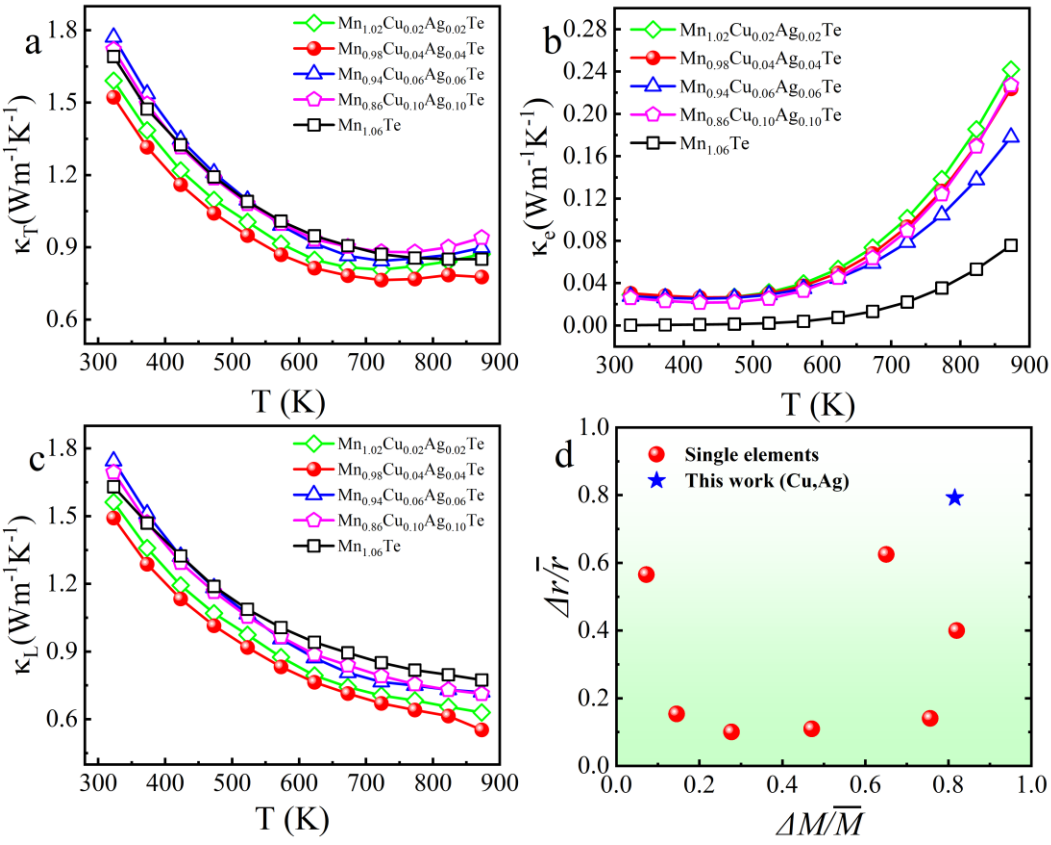

Figure. 5. Microstructural characterization of $Mn_{0.98}Cu_{0.04}Ag_{0.04}Te$:(a) Typical HAADF-STEM image showing the distribution of plenty nanoprecipitates.(b) An enlarged view of the zone in the yellow rectangle in Figure 5a. (b1-b4) Elemental mappings of nanoparticles taken from (b). (c) Atomic resolution HAADF-STEM image of nanoprecipitates. (d) Image showing dislocations in the matrix phase. (e,) HAADF-STEM images showing details of lattice distortions in matrix phase and (f) the corresponding strain mapping.

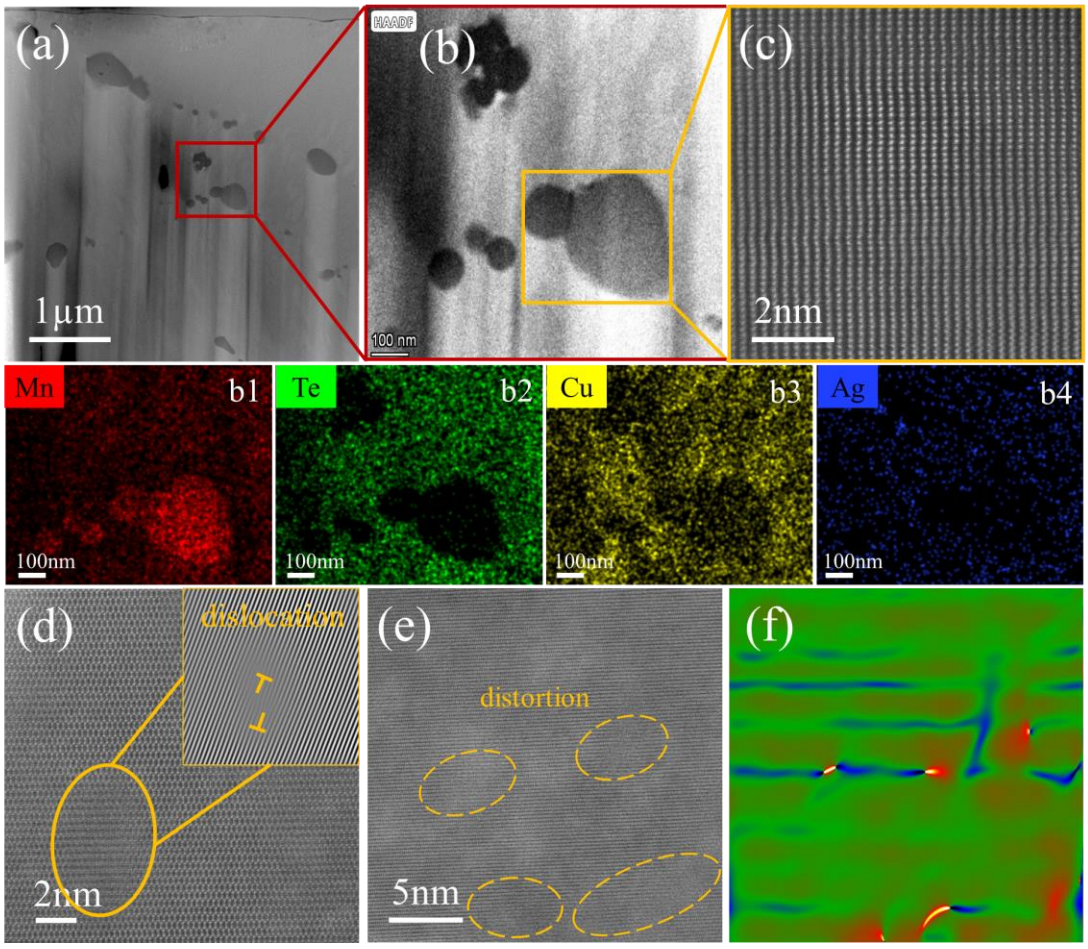

Figure. 6. (a) Temperature-dependent ZT values for $Mn_{1.06}Te$ and $Mn_{1.06-2x}Cu_xAg_xTe$ samples; (b) Comparison of peak *ZT* with other reported MnTe systems including MnTe-0.5% Na_2S, MnTe-0.75% Na, $Mn_{0.93}Ag_{0.07}Te$, $MnTe_{0.92}Se_{0.08}$, MnTe- 4% Ag_2S, MnTe-1.5% Sb_2Te_3.